Saturation Recovery Single-Shot Acquisition (SASHA) for Myocardial T_1 Mapping

Kelvin Chow,[1] Jacqueline A. Flewitt,[2,3] Jordin D. Green,[4] Joseph J. Pagano,[1] Matthias G. Friedrich,[2,3] and Richard B. Thompson[1]*

Purpose: To validate a new saturation recovery single-shot acquisition (SASHA) pulse sequence for T_1 mapping and to compare SASHA T_1 values in heart failure patients and healthy controls.

Theory: The SASHA sequence consists of 10 electrocardiogram-triggered single-shot balanced steady-state free precession images in a breath-hold. The first image is acquired without magnetization preparation and the remaining nine images follow saturation pulses with variable saturation recovery times.

Methods: SASHA was validated through Bloch equation simulations, Monte Carlo simulations, and phantom experiments. Pre- and postcontrast myocardial and blood T_1 values were measured in 29 healthy volunteers and 7 patients with heart failure.

Results: SASHA T_1 values had excellent agreement (bias, 5 ± 5 ms) with spin echo experiments in phantoms with a wide range of physiologic T_1 and T_2 values and its accuracy was independent of flip angle, absolute T_1, T_2, and heart rate. The average baseline myocardial T_1 in heart failure patients was higher than in healthy controls (1200 ± 32 vs. 1170 ± 9 ms, $P < 0.05$) at 1.5T, as was the calculated blood–tissue partition coefficient, λ, (0.42 ± 0.04 vs. 0.38 ± 0.02, $P < 0.05$), consistent with diffuse myocardial fibrosis.

Conclusions: The SASHA sequence is a simple and fast approach to in vivo T_1 mapping with good accuracy in simulations and phantom experiments. **Magn Reson Med 71:2082–2095, 2014. © 2013 Wiley Periodicals, Inc.**

Key words: T_1 mapping; myocardial fibrosis; saturation recovery; myocardium; magnetic resonance imaging; tissue characterization

Quantitative myocardial T_1 mapping, performed either pre- or postgadolinium contrast administration, has proven to be an invaluable tool in the noninvasive assessment of cardiac remodeling. Increased noncontrast myocardial T_1 values have been related to the extent of tissue damage in acute myocardial infarction (1), whereas shortened postcontrast T_1 values from higher tissue gadolinium concentrations have been used to detect increased extracellular volume. In diseases with diffuse myocardial fibrosis, such as patients following heart transplantation (2), with aortic stenosis (3), and with hypertrophic cardiomyopathy (3), postcontrast myocardial T_1 values have shown good correlation with histological measures of fibrosis including biopsy measurements of myocardial collagen content (2) and collagen volume fraction (3).

However, postcontrast myocardial T_1 values are sensitive to both the time of measurement after contrast delivery (3–6) and the amount of contrast administered. The blood–tissue partition coefficient, λ, is the ratio of tissue contrast concentration to the blood concentration, and more accurately reflects the underlying tissue extracellular volume fraction. Tissue and blood contrast concentration can be derived using changes in T_1 from baseline to postcontrast delivery (7). As λ is calculated using blood and tissue T_1 values before and after contrast, T_1 imaging sequences used for the measurement of λ should be accurate over the wide range of T_1 and T_2 values found in blood and tissue both pre- and postcontrast.

Inversion recovery sequences are commonly used for T_1 mapping owing to their use of the full dynamic range of signal intensities, but conventional methods require full T_1 recovery between acquisition and subsequent inversion pulses and thus total acquisition times are too long for breath-hold imaging. Look–Locker techniques (8) allow for faster imaging with continuous fast low angle shot (FLASH) (9–11), echo planar imaging (12), or balanced steady state free precession (bSSFP) (13) readouts following a single inversion pulse. A correction factor (9) is used to account for magnetization attenuation owing to image acquisition in these techniques. Electrocardiogram (ECG) triggering allows for cardiac T_1 mapping with Look–Locker techniques; however, combining data from multiple cardiac phases (11) may introduce errors owing to through-plane motion.

The MOdified Look–Locker Inversion (MOLLI) recovery sequence (6,14,15) consists of several "Look–Locker" sets, each containing several ECG-triggered single-shot images at the same cardiac phase in sequential heartbeats following a single inversion pulse. The MOLLI sequence, and its shorter breath-hold variants using different image sampling schemes (5,16), has been used to calculate

[1]Department of Biomedical Engineering, Faculty of Medicine and Dentistry, University of Alberta, Edmonton, Canada.

[2]Stephenson Cardiovascular Centre, Libin Cardiovascular Institute of Alberta, University of Calgary, Calgary, Canada.

[3]Marvin Carsley CMR Centre, Montreal Heart Institute, Université de Montréal, Montreal, Canada.

[4]Siemens Healthcare, Calgary, Alberta, Canada.

*Correspondence to: Richard B. Thompson, Ph.D., Department of Biomedical Engineering, 1082 Research Transition Facility, University of Alberta, Edmonton, AB, Canada T6G 2V2. E-mail: richard.thompson@ualberta.ca
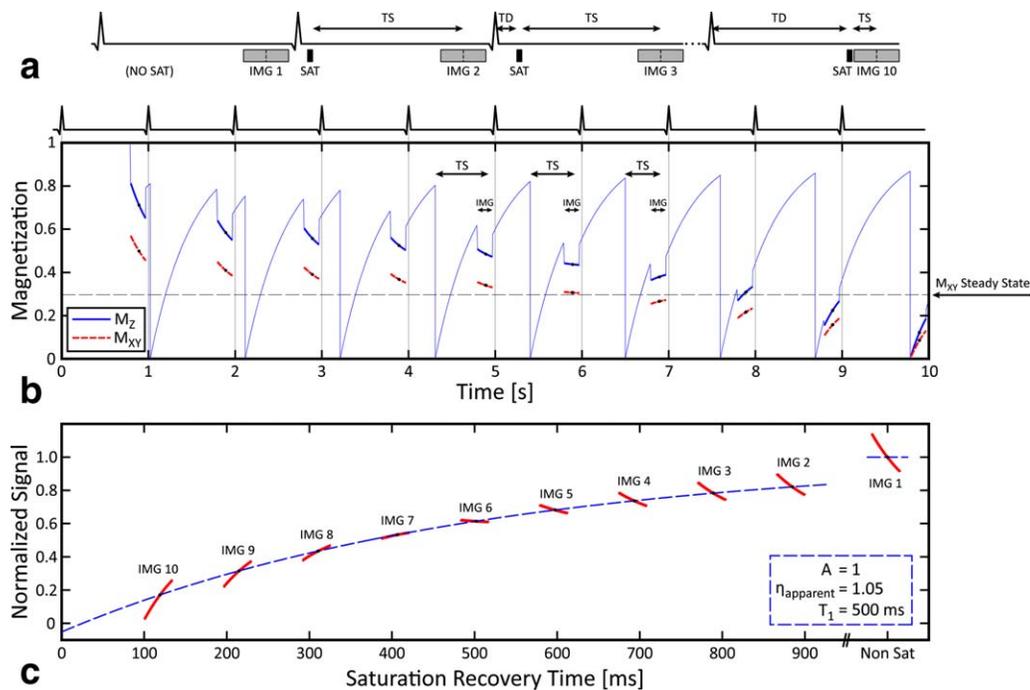
FIG. 1. **a:** Schematic diagram of the SASHA pulse sequence showing variable saturation recovery times (TS) between saturation (SAT) and each image readout (IMG). Variable trigger delays are used to maintain constant cardiac phase for all images. Dashed vertical lines within each image readout represent the center of k-space. **b:** Bloch equation simulation of longitudinal (M_Z) and transverse (M_{XY}) magnetization during the SASHA sequence for postcontrast blood with $T_2/T_1 = 180/500$ ms and ideal saturation ($\eta_{actual} = 1$). Bold lines indicate magnetization during imaging. **c:** Magnetization curves for all images from (b) are shown scaled down in time by a factor of 5 and normalized to the signal intensity of the first image. The best-fit of Eq. 2 through the center of k-space for each image is shown with a dashed line. [Color figure can be viewed in the online issue, which is available at wileyonlinelibrary.com.]

myocardial and blood T_1 values in healthy volunteers (5,6,16), patients with myocardial infarction (17,18), chronic aortic regurgitation (19), and those with nonischemic late enhancement lesions (18). However, MOLLI sequences underestimate T_1 values by 4–10% in phantom studies (14–16) and are known to have greater underestimation in short T_2 tissues such as the myocardium (20,21). Saturation recovery variants of MOLLI have been developed but also have a systematic underestimation of ~5% (22), likely owing to a similar magnetization attenuation effect from multiple image readouts after a single preparation pulse. Saturation recovery imaging with a single gradient echo image per saturation pulse, eliminating the magnetization attenuation effects in MOLLI approaches, has also been demonstrated in vivo (23,24). However, gradient echo readouts are limited by both poor overall signal to noise (SNR) and poor blood–tissue contrast compared to the bSSFP readout used in MOLLI.

We present a similar saturation recovery single-shot acquisition (SASHA) sequence for T_1 mapping using a single-shot bSSFP readout to provide good SNR and blood–tissue contrast. We propose that this approach will overcome the limitations of bSSFP Look–Locker sequences, where factors such as T_2 and heart rate affect the accuracy of calculated T_1 values in a complex manner. Accuracy of SASHA-derived T_1 values and their dependence on T_1, T_2, flip angle, off-resonance, heart rate, SNR, and saturation efficiency were evaluated using numerical simulations and validated in NiCl$_2$-agarose phantoms.

The dependence of myocardial T_1 and λ on the time following contrast agent administration was characterized in a group of healthy volunteers. T_1 and λ values were also measured in patients with heart failure, a disease where diffuse fibrosis has been described previously (25,26) and measured (2), and compared to a control group. Measurement reproducibility for in vivo studies was characterized with inter- and intraobserver variability statistics.

THEORY

The SASHA pulse sequence consists of 10 single-shot bSSFP images acquired over consecutive heartbeats, where the first image is acquired without magnetization preparation and the remaining images follow saturation pulses with variable saturation recovery times (TS) that uniformly span the R–R interval. TS is defined as the time from the end of the saturation radiofrequency (RF) pulse to the center line of k-space. Images are ECG-triggered and a variable trigger delay is added before each saturation pulse to obtain a consistent cardiac phase (diastasis) for all images (Fig. 1a).

The saturation recovery preparation results in a starting magnetization for each SASHA image (other than the first) defined by:

$$M(0) = 1 - \eta_{actual} e^{-(TS-\Delta)/T_1} \qquad [1]$$

where η_{actual} is the saturation pulse efficiency ($\eta_{actual} = 1$ for perfect saturation) and Δ is the time from the start

of imaging to the center of k-space. This magnetization is further modulated by multiple bSSFP RF pulses during imaging as shown in Figure 1b. However, the relationship between signal intensity, TS, and T_1 can still be expressed using a three-parameter exponential recovery model, as derived analytically in the Appendix (Eq. A11):

$$\text{Signal} = A(1 - \eta_{\text{apparent}}e^{-TS/T_1}) \qquad [2]$$

where A is a scaling factor and η_{apparent} is the apparent saturation efficiency, which is η_{actual} multiplied by a constant determined by acquisition parameters as detailed in Eq. A13. The overall effect of the bSSFP readout is an apparent change in saturation efficiency and scaling factor, whereas the exponential T_1 term remains unaffected. Changes in flip angle and the distribution of flip angles with realistic slice profiles both result in changes in η_{apparent} and the scaling factor, whereas the T_1 term is again unaffected as discussed in Appendix.

METHODS

Pulse Sequence

The SASHA pulse sequence was implemented on a 1.5T MRI scanner (Avanto; Siemens Healthcare; Erlangen, Germany). Typical sequence parameters were composite saturation with three RF pulses, 70° flip angle, three preparation ramped start-up RF pulses with flip angle scaling factors of 1/6, 3/6, and 5/6 (of 70°), a closing $\alpha/2$ (35°) RF pulse following imaging, 1.3 ms echo time (TE), 2.6 ms repetition time (TR), 119–885 ms TS (for a heart rate of 60 bpm), 8 mm slice thickness, 270 × 360 mm field of view, 108 × 192 acquisition matrix size before interpolation, 75% phase resolution, and rate 2 parallel imaging [generalized auto-calibrating partially parallel acquisition (GRAPPA)] for a ~175 ms imaging window. All imaging was performed with body coil RF transmission.

Calculation of T_1 Values

T_1 image analysis was performed offline using MATLAB R2009a (The MathWorks; Natick, MA). For all simulations, phantom, and in vivo experiments, T_1 values were calculated by fitting image signal intensities to a three-parameter exponential recovery curve (Eq. 2). The first nonsaturated image had the exponential term set to zero so that Signal $= A$. A Levenberg–Marquardt algorithm (27) was used to determine best-fit values for A, η_{apparent}, and T_1.

Simulations

The full SASHA pulse sequence was simulated using the Bloch equations in MATLAB with actual acquisition and timing parameters. Saturation pulses were implemented as complete spoiling of transverse magnetization and multiplication of longitudinal magnetization by $(1 - \eta_{\text{actual}})$. Simulations were performed using ranges of heart rates (60–100 bpm), T_1s (300–2000 ms), T_2s (50–250 ms), η_{actual} (0.9–1.1), flip angles (30–90°), and off-

resonant frequencies ($\pm 0.375/\text{TR}$, i.e., ± 143 Hz) to determine the dependence of best-fit T_1 values on each parameter. Signal intensities from simulations with different flip angles were also combined as a weighted sum before calculating T_1 to emulate the effect of an excitation slice profile.

The range of SASHA TS times is determined by the R–R interval, where the sampling of the recovery curve will be reduced at higher heart rates and more so for longer T_1 values. Monte Carlo simulations were performed to examine the noise dependence of best-fit T_1s for blood (precontrast T_2/T_1: 240/1650 ms, postcontrast: 180/500 ms) and myocardium (precontrast T_2/T_1: 50/1175 ms, postcontrast: 50/725 ms). T_1s were selected to reflect baseline (noncontrast) T_1 values and those 15 min after a 0.1 mmol/kg bolus of a gadolinium. Noncontrast T_2s were selected based on the literature values (28), and postcontrast T_2s were calculated using the relaxivity equation, assuming matching relaxivity for T_1 and T_2. For each case, simulations were run with 100,000 repetitions for heart rates of 60 and 100 beats per minute (bpm) and SNR values of 20–120 in steps of 10. Simulated signal intensities were calculated using the Bloch equations with TS times matching those calculated on the MRI scanner for the given heart rate and signal intensity was normalized to unity at the nonsaturated time point. In each repetition, T_1 values were calculated using Rician-distributed data with ν as normalized simulated signal intensities and σ as 1/SNR to represent magnitude reconstructed data. Based on this definition, the nonsaturated image has the specified SNR value and remaining nine SASHA images have lower SNR values owing to reduced signal intensities, as determined by the TS time. The distributions of best-fit T_1 values are presented as normalized T_1 error (i.e., divided by the input T_1) to facilitate comparison between blood and tissue simulations with different input T_1 values. Variability and bias in best-fit T_1 errors are reported as the interquartile range (IQR) of normalized T_1 values and median of normalized T_1 values, respectively.

Phantom Experiments

The accuracy of SASHA-derived T_1 values was evaluated in 14 NiCl$_2$-doped agarose phantoms (29) with T_1 and T_2 values spanning the wide range found in blood and myocardium with a normal range of gadolinium concentrations. Gold standard T_1 measurements were performed using inversion recovery spin echo experiments with 15 inversion times spanning 100–3000 ms, 11 ms TE, and one line of k-space acquired per inversion. Gold standard T_2 measurements were performed with spin echo experiments with 7 TEs spanning 11–200 ms, acquired in separate acquisitions. Common sequence parameters between all spin echo imaging were 10 s TR, 129 × 360 mm field of view, 46 × 128 matrix size, 8 mm slice thickness, and a 90° excitation flip angle. Inversion recovery data were fit to Eq. 2 to determine T_1, whereas multiple TE data were fit to $S = A \exp(-TE/T_2)$ to determine T_2.

The experimentally achieved saturation efficiency (η_{actual}) was measured in phantoms using saturation recovery gradient echo images, acquired with one line of

k-space per saturation pulse, with four images with TS times (3, 45, 87, and 129 ms) and one image without saturation for a total of five images. Pulse sequence parameters were 15° flip angle, 2.12 ms TE, 180 × 360 mm field of view, 64 × 128 matrix size, 8 mm slice thickness, and 10 s TR. Signal intensity was fit to Eq. 2 and best-fit $\eta_{apparent}$ was taken to be η_{actual}.

SASHA T_1 mapping was performed using a simulated heart rate of 60 bpm and other acquisition parameters as described above. All phantoms were imaged using a 16-element posterior body coil. T_1, T_2, and η_{actual} values were calculated for each pixel within a region of interest (ROI) in each phantom using a Levenberg–Marquardt algorithm.

In Vivo Studies

All subjects provided written informed consent with study approval from the University of Calgary Conjoint Health Research Ethics Board. Myocardial and blood T_1 values were measured in a mid-ventricular short-axis slice using SASHA with ECG-triggered diastasis imaging in a 10-heartbeat end-expiration breath-hold. All in vivo imaging was performed using a 32-element (16 anterior and 16 posterior) body coil.

In a postcontrast time-course substudy, SASHA T_1 measurements were obtained at baseline and every 1–4 min up to 15 min following a bolus injection of 0.1 mmol/kg gadolinium-diethylenetriaminepentaacetic acid (Gd-DTPA, Magnevist; Bayer Healthcare, Toronto, Canada) in 19 healthy subjects without a history of heart disease. Slice thickness was 8–10 mm with other SASHA acquisition parameters the same as above.

In a patient substudy, nine consecutive heart failure patients and 10 consecutive healthy control subjects from an ongoing clinical study of heart failure (Alberta HEART, Alberta Heart Failure Etiology and Analysis Research Team) had SASHA T_1 measurements performed with acquisition parameters as above. T_1 measurements were obtained at baseline and approximately 25 min following 0.15 mmol/kg gadobutrol (Gadovist; Bayer HealthCare Pharmaceuticals, Montville, NJ). Standard phase-sensitive inversion recovery late gadolinium enhancement imaging (30) was used to identify focal scaring and a short-axis stack of bSSFP cine images was used to calculate left-ventricular mass, volume, and ejection fraction with standard method of disks volumetric analysis using cmr[42] (Circle Cardiovascular Imaging, Calgary, Canada).

In Vivo Image Analysis

Saturation efficiency and T_1 image analysis was performed offline by a single individual (KC) using MATLAB. A nonrigid image registration algorithm (31) was used to coregister all 10 images within each SASHA data set. Endocardial and epicardial borders were manually traced on the coregistered images with the inferior right ventricular insertion point identified as a reference point to divide the myocardium into 18 equal circumferential segments, corresponding to each of the six mid-ventricular AHA standardized segments (32) subdivided into three. Images with ECG mistriggering or residual

motion following coregistration were excluded from analysis, with T_1 and λ calculated using the remaining SASHA images. Segments with artifacts or partial voluming of the myocardium were excluded from further analysis and segments with focal scarring identified in late enhancement images (in the patient substudy) were analyzed separately. An ROI within the left ventricular cavity was traced for blood pool T_1 measurements.

The blood–tissue partition coefficient, λ, was obtained by normalizing the tissue contrast concentration to the blood concentration, where concentration was calculated using the change in T_1 from baseline to postcontrast delivery in both blood and tissue (7):

$$\lambda = \frac{R_1(\text{myocardium}_{post}) - R_1(\text{myocardium}_{pre})}{R_1(\text{blood}_{post}) - R_1(\text{blood}_{pre})},$$

$$\text{where } R_1 = \frac{1}{T_1} \qquad [3]$$

Myocardial and Blood T_1 Variability

Variability in precontrast T_1 values was characterized by calculating a parametric T_1 map for all myocardial and blood pixels using the coregistered SASHA images. The IQR of pixel T_1 values in each myocardial and blood ROI was normalized to the median T_1, as true "input" T_1 values are not known in vivo. These values were compared with the IQR of normalized T_1 values from Monte Carlo simulations.

Inter- and Intraobserver Reproducibility

Myocardial and blood contours for all subjects were redrawn after at least 1 month by KC at both the precontrast and the postcontrast time points (at only 15 min for time-course subjects) to assess intraobserver variability. All analysis was repeated by a second observer (RBT) to assess interobserver variability.

Statistics

Myocardial T_1, λ, and T_1 variability for each subject was calculated as the average of these values from all included segments without focal scar in late enhancement imaging. Group values are expressed as mean ± standard deviation. Multiple regression analysis was used to determine the effects of gender and heart rate on precontrast myocardial and blood T_1 values in the postcontrast time-course substudy population. Student's t-tests were used for statistical comparison of λ and T_1 between heart failure and control groups in the patient substudy. Paired Student's t-tests were used for statistical comparison of λ and T_1 between scarred and remote segments in subjects with focal scarring. Inter- and intraobserver variability was assessed using the coefficient of variation (CV) (standard deviation of the differences divided by the mean) and intraclass correlation (ICC) using a two-way random effects model with absolute agreement for single measurements. The distribution of best-fit T_1 values was tested for normality using the Lilliefors test. Statistical tests were performed using SPSS version 19 (IBM Software Group,
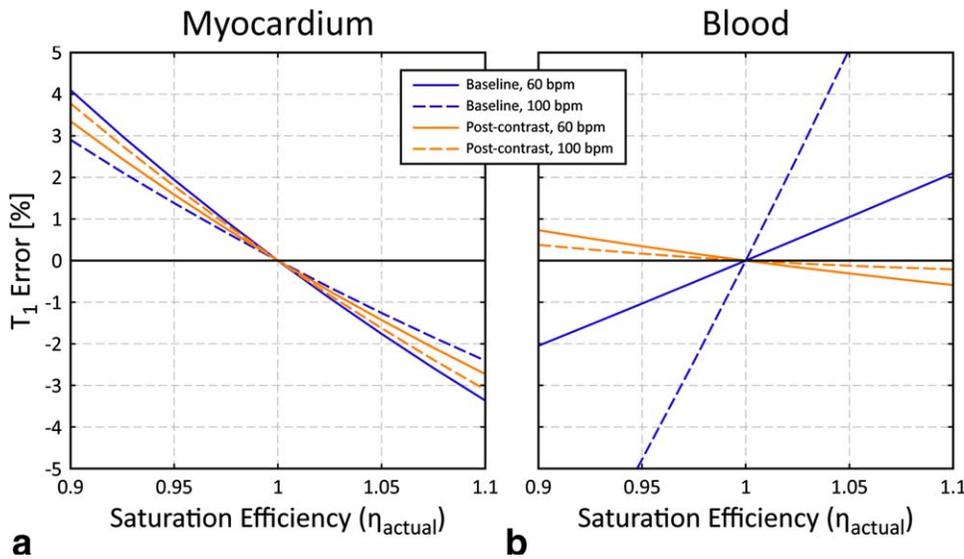
FIG. 2. Error in SASHA-derived T_1 values with imperfect saturation pulses in the myocardium (**a**) and blood (**b**), calculated using Bloch equation simulations. [Color figure can be viewed in the online issue, which is available at wileyonlinelibrary.com.]

Somers, USA) with statistical significance set at $P < 0.05$ for all tests.

RESULTS

Simulations

Figure 1b shows the longitudinal and transverse magnetization from a SASHA Bloch equation simulation with the following input parameters: no added noise, ideal saturation pulses, on-resonance, 60 bpm heart rate, 500 ms T_1, and 180 ms T_2, reflecting postcontrast blood relaxation values. Abrupt changes observed in longitudinal magnetization before and after imaging are owing to the start-up RF pulses and the $\alpha/2$ closing pulse, respectively. The large signal variation over each single-shot acquisition depends on the initial magnetization (determined by TS) relative to the steady-state value (determined by T_1, T_2, and various pulse sequence parameters (33)).

The transverse magnetization curves from each image acquisition in the simulation are shown again in Figure 1c, ordered by TS, and scaled in time by a factor of 5 to fit on the time scale. The best-fit curve of signal intensities at center k-space to Eq. 2 is also shown, with the calculated T_1 exactly matching the input T_1. The calculated apparent partial inversion ($\eta_{apparent} = 1.05$), despite the use of ideal saturation pulses, is owing to the magnetization perturbation by the bSSFP readout, as described in Appendix. Additional simulations with ideal saturation and every combination of heart rates, T_1s, T_2s, flip angles, and off-resonant frequencies up to $\pm 0.25/TR$ (± 96 Hz), as detailed in the Methods section, all resulted in best-fit T_1 errors $<0.5\%$. For off-resonant frequencies between $\pm 0.25/TR$ and $\pm 0.375/TR$ (± 143 Hz) best-fit T_1 errors were 5% or less in 99% of simulated parameter combinations, with errors reaching as high as 8% with flip angles of 90°. Simulations showed no best-fit T_1 dependence on flip angle distributions, resulting from realistic slice excitation profiles, as expected from Eq. A15.

Numerical simulations with nonideal saturation pulses showed small systematic errors in best-fit T_1 values, likely as a result of residual magnetization carried over between heartbeats. Figure 2 shows T_1 error as a function of η_{actual} and heart rate for pre- and postcontrast blood and myocardium, with true T_1 and T_2 values as described for Monte Carlo simulations in **METHODS** section. The magnitude and direction (underestimation or overestimation) of the errors were different for blood and myocardium and also different with contrast. T_1 errors were mostly insensitive to heart rate, except for precontrast blood where larger errors were found at a high heart rate of 100 bpm. All other errors were less than $\sim4\%$ for the range of $\eta_{actual} = 0.9$–1.1.

Figure 3 shows box plots of distributions of normalized best-fit T_1 errors from Monte Carlo simulations, as a function of SNR in the nonsaturated SASHA image. Nearly, all (150 out of 152) combinations of heart rate, input T_1/T_2 values, and SNR resulted in non-normal distributions as determined by the Lilliefors test, with increasing skewness at lower SNRs and visualized by the unequal halves of boxes in Figure 3. However, for SNR values >50 at a heart rate of 60 bpm, distributions were approximately normal and the CV could be approximated as normalized IQR divided by 1.35 with an error of $<1\%$ from the true CV. Median and IQRs for simulations of precontrast myocardium and blood are replotted in Figure 4 to allow for better visualization of bias and variability as a function of SNR. The IQR (variability) increased with decreasing SNR, but is overall larger in precontrast simulations, particularly in the blood at higher heart rates. Nonzero median T_1 errors indicate systematic overestimation of best-fit T_1 values following a similar trend, with appreciable overestimation in baseline blood T_1 values at 100 bpm and an SNR of 20 in the nonsaturated SASHA image.

Phantom Experiments

The mean and standard deviation of T_1 and T_2 values calculated from the reference spin-echo experiments for
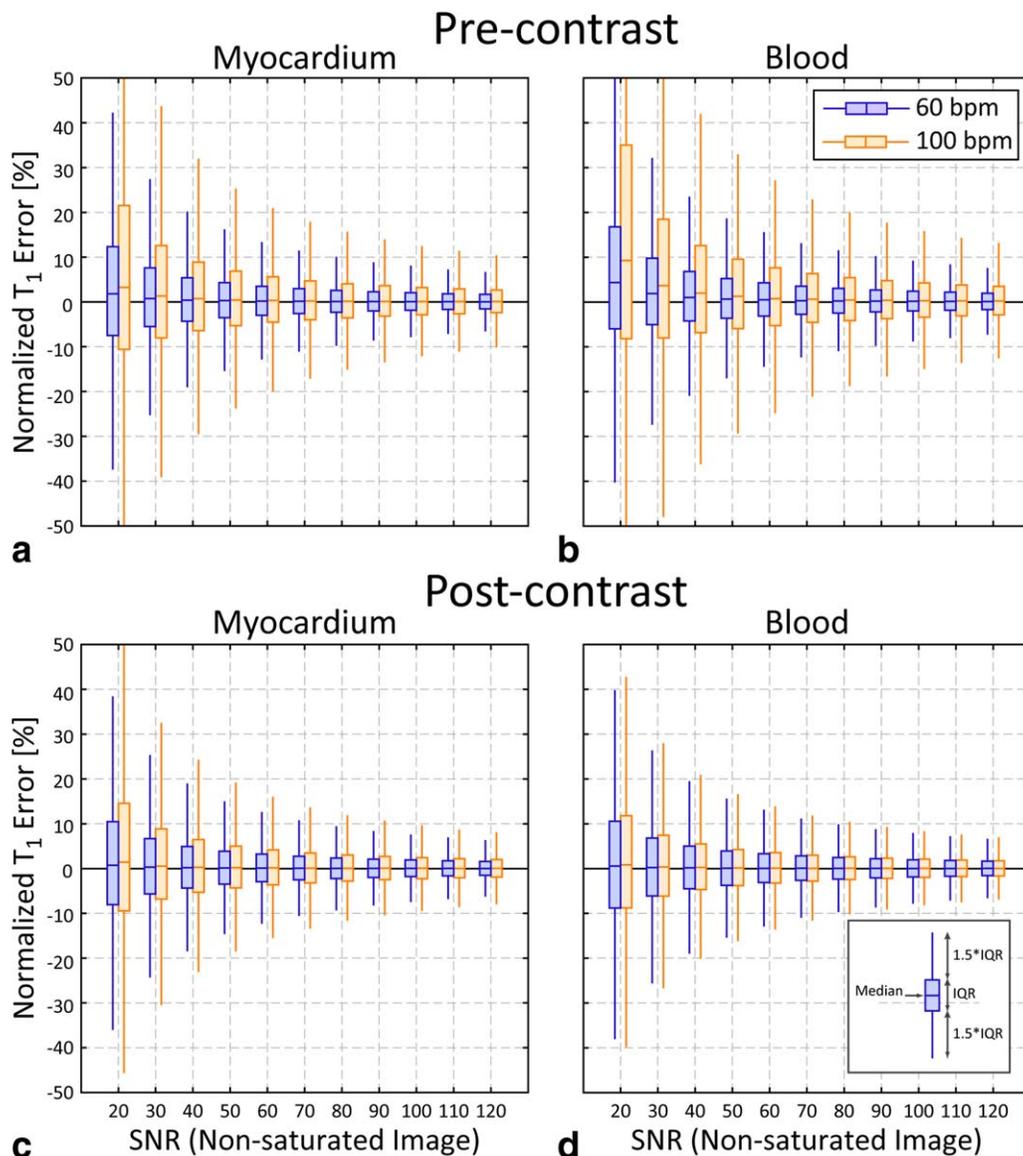
Pre-contrast

FIG. 3. Box-and-whiskers plot of Monte Carlo simulations results using T_1/T_2 values representing myocardium (left) and blood (right) at baseline (top) and 15-min postcontrast (bottom) as a function of SNR values in nonsaturated image. Plotted boxes indicate the median and IQR, whereas whiskers indicate the nonoutlier bounds (furthest data points within 1.5 IQR of the upper and lower quartiles). [Color figure can be viewed in the online issue, which is available at wileyonlinelibrary.com.]

all phantoms are listed in Table 1. Phantoms 1–8 had T_1 and T_2 values similar to in vivo myocardial tissue, whereas phantoms 9–14 had values similar to blood. Bland–Altman analysis of SASHA T_1 values compared to gold standard spin-echo T_1 values showed a small positive bias of 5 ± 5 ms with no significant trend. Errors in SASHA T_1 values did not show significant correlation with absolute T_1 or T_2 values. Excellent saturation efficiency was obtained in the phantoms, with a measured η_{actual} of 0.995 ± 0.004 over pixels within all 14 phantoms.

In Vivo Studies

Two heart failure patients were excluded for poor image quality; all remaining subjects from both time course and patient substudies had analyzable SASHA T_1 data. One excluded patient had ghosting artifacts that obscured the majority of the left ventricle, and the second patient had severe ECG mistriggering. Patient characteristics and imaging results for remaining subjects are summarized in Table 2.

Breath-holds averaged 10 ± 2 s and were well tolerated in all subjects. ECG mistriggering or motion uncorrectable by image registration resulted in the exclusion of 8 out of 2730 images in 273 analyzed SASHA data sets. The presence of artifacts resulted in the exclusion of 3% of segments in the postcontrast time-course substudy subjects, and 9% in controls and 8% in heart failure patients in the patient substudy. In total, 67% of excluded segments were located in the anterior or inferolateral regions. The most common reason for segment exclusion was partial voluming of the myocardium although occasional ghosting over the myocardium was also found in larger subjects.
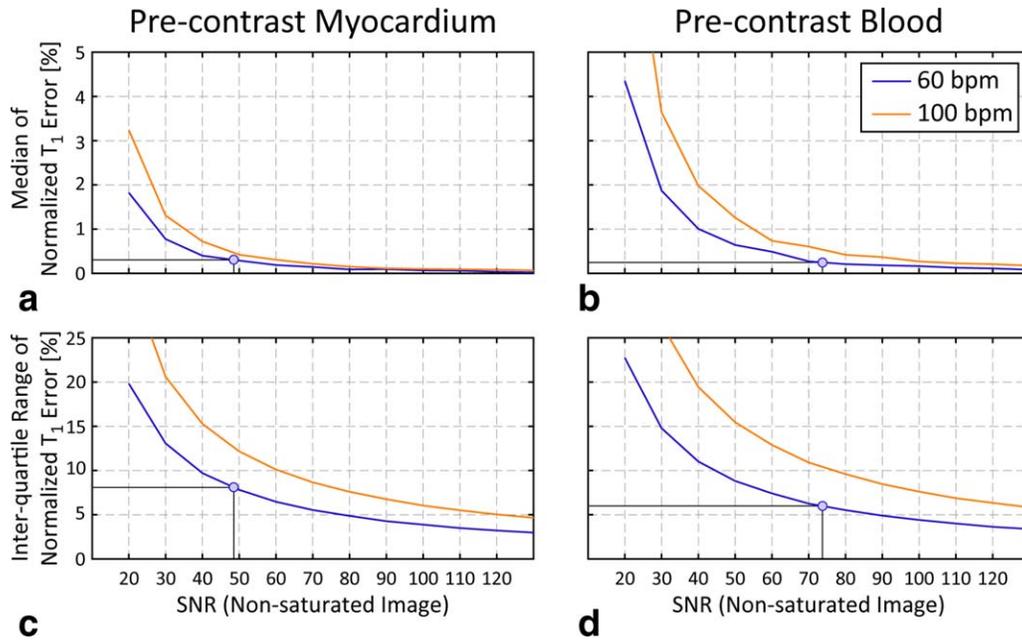
FIG. 4. Median (top) and IQR (bottom) of Monte Carlo simulation results using T_1/T_2 values representing precontrast myocardium (left) and blood (right). Plotted data points indicate the measured normalized IQR from in vivo data and the corresponding SNR and median normalized T_1 error. [Color figure can be viewed in the online issue, which is available at wileyonlinelibrary.com.]

Positive late enhancement was found in 16% of segments for the heart failure patients and not found in any segments for the control subjects.

Figure 5a shows images at several TS times in a healthy subject precontrast along with myocardial segmentation contours. Good blood–tissue contrast is seen in the nonsaturated image, but with reduced contrast at the endocardial border in saturation prepared images, typical of precontrast imaging. A typical best-fit recovery curve from a mid-septal segment is shown in Figure 5b alongside a bull's-eye plot representing all myocardial and blood pool T_1 values from ROI analysis (Fig. 5c). A

difference in best-fit $\eta_{apparent}$ between myocardial and blood recovery curves is owing to their difference in T_1 and T_2 values as described in Appendix. A pixel-by-pixel parametric T_1 map is shown in Figure 5d. The average myocardial T_1 value of the 18 circumferential segments (1175 ± 32 ms) was similar to the average T_1 value of individual pixels over entire myocardium (1179 ± 58 ms).

SASHA images in a heart failure subject 33 min following contrast (Fig. 6a) show good blood–tissue contrast in all images, typical of postcontrast imaging. Reduced postcontrast myocardial T_1 values in a bull's-eye plot (Fig. 6b) and pixel T_1 map (Fig. 6c) correspond to the transmural ischemic pattern scar in the inferior wall of the corresponding late enhancement image (white arrow, Fig. 6d).

The average normalized IQR of T_1 values within myocardial ROIs, excluding segments with artifact or positive late enhancement, was 8.8 ± 2.8% over all subjects (Table 2), with less variability in healthy subjects than heart failure patients. T_1 variability was less in the blood pool than in the myocardium, with an average normalized IQR of 7.3 ± 2.7% over all subjects.

Table 1
T_1 and T_2 Values of Agarose Phantoms, as Determined by Spin Echo and SASHA

| | Spin- Eecho | | SASHA |
Phantom number	T_2 [ms]	T_1 [ms]	T_1 [ms]
Myocardial-like			
1	47.4 ± 0.2	1142 ± 4	1142 ± 19
2	58.0 ± 0.4	1154 ± 4	1159 ± 17
3	65.0 ± 0.6	1151 ± 5	1164 ± 22
4	74.5 ± 0.3	1154 ± 4	1160 ± 15
5	46.2 ± 0.3	963 ± 4	966 ± 18
6	45.2 ± 0.4	738 ± 3	741 ± 14
7	44.0 ± 0.3	602 ± 3	605 ± 13
8	50.0 ± 0.3	342 ± 2	344 ± 8
Blood-like			
9	172.4 ± 0.9	1470 ± 6	1466 ± 23
10	117.8 ± 0.4	279 ± 1	279 ± 5
11	165.5 ± 0.6	435 ± 1	440 ± 5
12	189.4 ± 0.7	606 ± 2	611 ± 9
13	177.6 ± 0.9	832 ± 3	848 ± 16
14	187.4 ± 0.9	991 ± 3	997 ± 18

Postcontrast Time-Course Substudy

The time course of blood T_1, myocardial T_1, and λ values after contrast injection is shown in Figure 7. The mean and standard deviation for all values are shown in 1-min intervals after contrast injection. Derived λ shows no significant trend from 5 to 15 min with an average value of 0.38 ± 0.01, whereas blood and tissue T_1s increase considerably by 29 and 17%, respectively, over the same interval.

Baseline blood T_1 values from the time-course substudy were not significantly related to heart rate when

Table 2
Subject Characteristics

	Time-course sub-study	Patient sub-study	
		Control	Heart failure
Male/Female	11/8	6/4	6/1
Age (years)	28 ± 6	54 ± 6	65 ± 9
Weight (kg)	73 ± 14	83 ± 20	87 ± 17
Heart rate (bpm)	65 ± 11	63 ± 8	71 ± 18
Left ventricle			
End-diastolic volume (mL/m²)		65 ± 9	96 ± 33
End-systolic volume (mL/m²)		24 ± 4	57 ± 31
Stroke volume (mL/m²)		41 ± 6	39 ± 6
Ejection fraction (%)		63 ± 4	43 ± 10
Myocardial T_1 (ms)			
Baseline	1174 ± 27	1170 ± 9	1200 ± 34[a]
Post 0.1 mmol/kg Gd-DTPA	720 ± 48		
Post 0.15 mmol/kg gadobutrol		568 ± 40	538 ± 32
Blood T_1 (ms)			
Baseline	1655 ± 86	1613 ± 93	1678 ± 127
Post 0.1 mmol/kg Gd-DTPA	498 ± 42		
Post 0.15 mmol/kg gadobutrol		335 ± 44	340 ± 37
Normalized IQR (%)			
Baseline myocardial T_1	7.2 ± 1.9	7.8 ± 2.1	11.0 ± 4.6
Baseline blood T_1	5.4 ± 1.5	5.5 ± 1.5	8.5 ± 3.2
Postcontrast time (min)	15 ± 1	24 ± 2	28 ± 4
Partition coefficient (λ)	0.38 ± 0.04	0.38 ± 0.02	0.42 ± 0.04[a]

LV = left ventricle; Gd-DTPA = gadolinium diethylenetriaminepenta-acetic acid. Reported LV volumes are indexed to body surface area.
[a]Statistical difference ($P < 0.05$) between the patients with heart failure and the control population.

controlling for gender from multiple regression analysis. However, a significant difference in baseline blood T_1 values was found between men (1605 ± 65 ms) and women (1724 ± 62 ms) when controlling for heart rate (mean 64 ± 13 bpm; range, 45–90 bpm). Baseline myocardial T_1 values showed no significant difference with gender or heart rate.

Heart Failure Substudy

Heart failure patients had reduced systolic function, larger end-diastolic volumes, and larger end-systolic volumes. Compared to controls, remote myocardial segments without focal scarring in heart failure patients had statistically higher precontrast myocardial T_1 values and increased λ, but postcontrast myocardial T_1 values were not statistically different (Table 2). In the four subjects with late enhancement focal scarring, scarred segments had statistically significantly higher precontrast myocardial T_1 values (1292 ± 33 vs. 1214 ± 34 ms), lower postcontrast myocardial T_1 values (483 ± 25 vs. 534 ± 25 ms), and significantly increased λ (0.54 ± 0.07 vs. 0.42 ± 0.04) compared to nonscarred segments.

Inter- and Intraobserver Reproducibility

Myocardial and blood T_1 measurements had excellent inter- and intraobserver coefficients of variation of <2.6% and ICCs of 1.00 for all. The derived partition coefficient (λ) had slightly higher inter- and intraobserver CV of 4.7 and 4.9%, respectively, and an ICC of 0.90 for both.

DISCUSSION

This study has described and validated a simple and accurate approach to blood and myocardial T_1 mapping that can be performed in a single 10-heartbeat breath-hold. Based on the numerical simulations and phantom experiments, the accuracy of SASHA T_1 values is independent of absolute T_1, T_2, heart rate, flip angle, and off-resonant frequencies up to ±96 Hz. Furthermore, best-fit T_1 values do not require a correction factor to account for magnetization attenuation by the imaging readout.

Myocardial and Blood T_1 Values

Baseline myocardial T_1 values in healthy subjects showed similar variability as other T_1 mapping techniques with an overall myocardial standard deviation of ±22 ms between subjects. Myocardial T_1 values in healthy subjects with SASHA (1174 ± 27 ms) are slightly lower than the previously reported values with a saturation recovery FLASH sequence (1219 ± 72 ms (23)) but considerably higher than values with MOLLI sequences (939 ± 24 ms (15), 947 ms (5), and 966 ± 48 ms (16)).

Baseline blood T_1 values in the time course and control subjects (1639 ± 97 ms) are also higher than the previously reported values using MOLLI (1518 ms (5)) and saturation recovery FLASH (1516 ± 21 ms (23)) sequences. Measurement of blood T_1 in these studies as well as in this study was performed within the left ventricular cavity where inflow errors may arise. In MOLLI sequences, the delay of several heartbeats between inversion and imaging for long TI images may cause distant noninverted blood to be imaged, resulting in an apparent decrease in T_1 values. Shorter TS times used in SASHA reduce the likelihood of nonsaturated blood being imaged, and thus inflow errors are expected to be diminished. Additionally, the previous studies have reported a considerable range of blood T_1 values in healthy subjects with a negative relationship between hematocrit and T_1 (34,35). This is consistent with the data from the time-course subjects in this study, where females had higher blood T_1 values compared to men (1724 ± 62 ms vs. 1605 ± 65 ms), likely as a result of the lower hematocrit values expected in women.

The difference in blood T_1 values between the SASHA and MOLLI sequences is consistent with a known 4–10% MOLLI T_1 underestimation in phantoms studies, with larger T_1 errors found at longer absolute T_1 values (14–16). The even larger difference in myocardial T_1 values can also be partially explained by the previous reports of greater MOLLI T_1 underestimation in short T_2 tissues such as the myocardium (20,21). However, almost 20% discrepancy observed for in vivo myocardial T_1 values requires further investigation. MOLLI sequences are also known to have heart rate dependencies that change
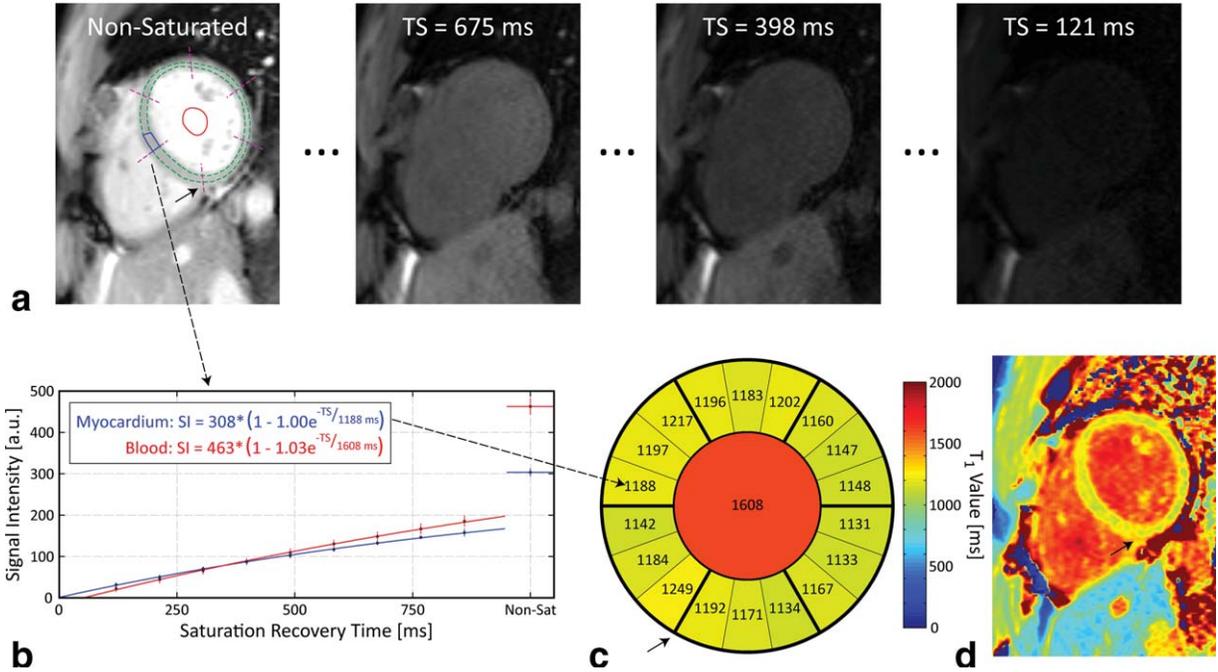
FIG. 5. T_1 mapping in a healthy time-course substudy subject before gadolinium contrast. **a**: SASHA images from a short-axis slice at various saturation recovery times along with myocardial (dashed circles) and blood contours (solid circle), inferior right ventricular insertion point (black arrow), and circumferential segmentation (dashed lines). **b**: Signal intensities from a septal segment (blue rectangle in (a)) and the blood pool ROI. Plotted circles and vertical lines indicate mean and ±2 standard deviations of signal intensities (in scanner units) within each ROI, respectively. Best-fit curves of Eq. 2 are also shown. **c**: T_1 values in the myocardium (circumferential segments) and blood pool (central circle). Black arrow indicates inferior right ventricular insertion point in (a, c, and d). **d**: Parametric T_1 map. Color map legend is matched between (c) and (d).
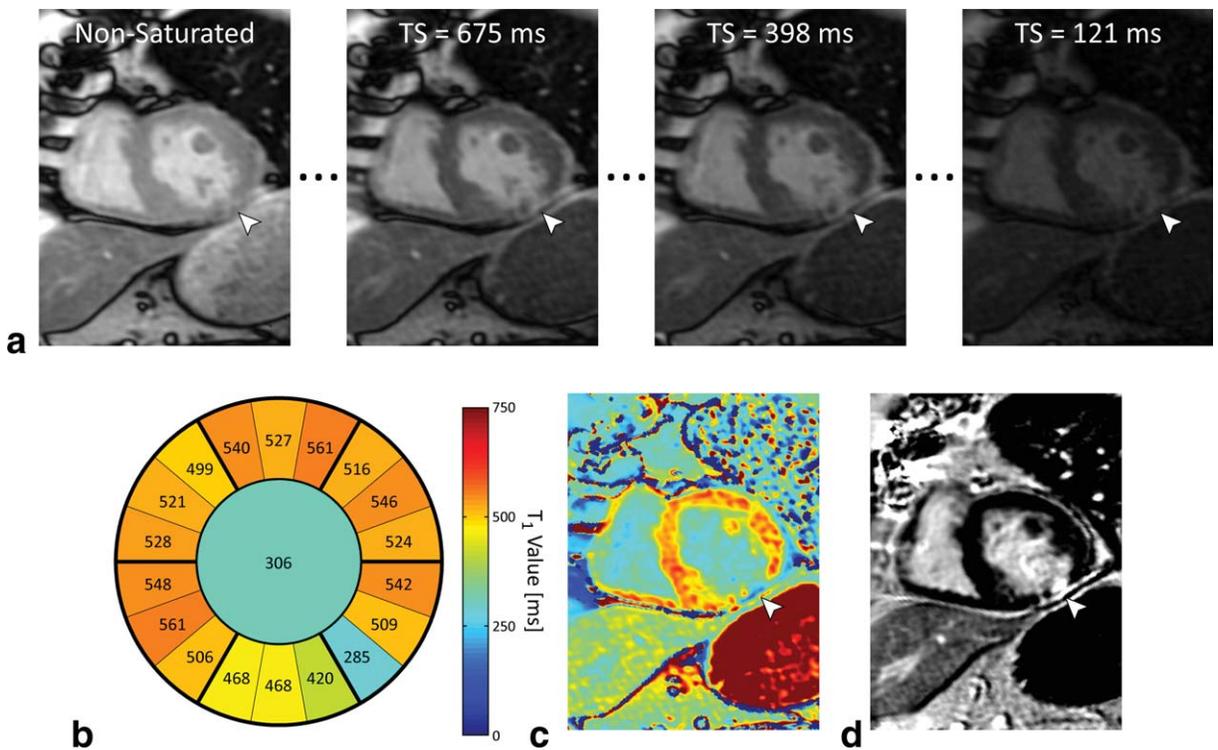
FIG. 6. T_1 mapping in a heart failure subject 33 min following contrast. **a**: SASHA images at various saturation recovery times with hyperintensity visible in the inferior wall (white arrow). A bull's-eye plot (**b**) of myocardial (circumferential segments) and blood (central circle) T_1 values and parametric T_1 map (**c**) both show reduced myocardial T_1 values in the inferior wall. **d**: Late gadolinium enhancement image showing transmural ischemic pattern scarring in the inferior wall (white arrow).
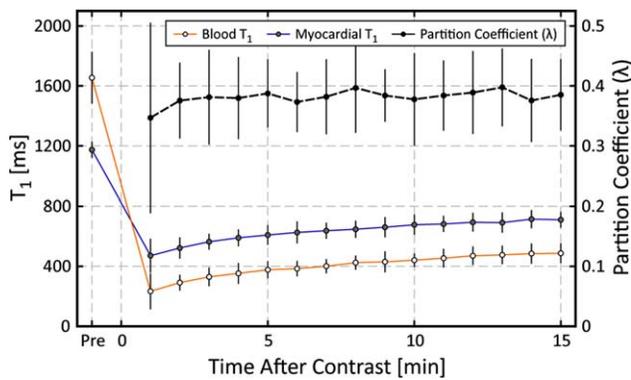
FIG. 7. Postcontrast time course of myocardial T_1, blood T_1, and partition coefficient (λ) in 19 healthy volunteers. Vertical lines represent two standard deviations above and below average values at each time point. [Color figure can be viewed in the online issue, which is available at wileyonlinelibrary.com.]

with the sampling scheme employed (5,16) although correction algorithms have been proposed (36). By comparison, the accuracy of SASHA T_1 values has been shown to be independent of absolute T_1s, T_2s, flip angle, and heart rates.

Partition Coefficient

In the postcontrast time-course subjects, λ remained constant, whereas myocardial and blood T_1 values increased with imaging time after contrast delivery as gadolinium was cleared from the blood and tissue. Insensitivity of λ with imaging time is consistent with the previous studies (4,5,11) and confirms λ as a more robust metric of the underlying extracellular volume fraction than postcontrast myocardial T_1 values alone. The dependence of postcontrast blood and tissue T_1 on measurement time observed in this study likely contributes to the lack of statistical significance in postcontrast myocardial T_1 values between the heart failure and the control group, despite a statistically higher λ in patients (Table 2). In particular, the later postcontrast imaging time in patients would result in an increase in postcontrast myocardial T_1 values that is independent of λ.

Heart failure patients had significantly higher λ in scarred segments compared to remote myocardium, consistent with replacement fibrosis, and higher λ in remote myocardium than controls, consistent with increased interstitial fibrosis expected in heart failure (26). Calculated λ was also similar in the healthy time-course and control populations, despite potential differences in myocardial T_1 values expected owing to dissimilar contrast agents, contrast dosage, and imaging times after contrast. However, direct comparison of these groups is confounded by age differences, as λ has been shown to change with age (18).

SASHA-derived λ-values for healthy subjects in this study (0.38 $\pm$ 0.04) are smaller than the previously reported values of 0.41 $\pm$ 0.06 using an IR-FLASH technique at 3T (11) and 0.43 $\pm$ 0.03 using a hybrid MOLLI technique with gadoteridol (5). Although λ reflects a physiologic parameter that is ideally independent of

measurement technique, comparisons of λ between studies are difficult owing to the propagation of sequence-dependent T_1 errors to the derived λ. In particular, T_2-dependent errors in MOLLI-derived T_1 values may result in systematic T_1 errors that are different in blood and myocardium owing to their different T_2 values. Also, although λ was similar between the two contrast agents used in this study, this may not hold true for all gadolinium-based contrast agents. Finally, reported changes in contrast agent relaxivity with field strength (37) may further confound direct comparisons.

Inter- and Intraobserver Reproducibility

Myocardial and blood T_1 measurements had low inter- and intraobserver coefficients of variation and excellent ICCs, similar to the previously reported values for MOLLI (38). Higher CVs and lower ICCs for the derived partition coefficient may be related to the reduced range of values for λ compared to the large range of T_1 values found pre- and postcontrast. ICCs for λ in this study were better than those previously reported for a study using the MOLLI sequence, where ICC was 0.82 using gadolinium-benzyloxypropionictetra-acetate (BOPTA) and 0.63 using Gd-DTPA (39). In all cases, the reproducibility CVs in this study were approximately half the variation found in each value for the healthy population.

Image Quality

A small percentage of myocardial sectors were excluded from the analysis owing to unclear boundaries of the myocardium with neighbouring blood or epicardial fat, both of which have greatly different T_1 values than myocardium. In ROI-based analysis where SNR is less of a limitation, reducing slice thickness may be useful by reducing partial voluming effects. As with any sequence using a bSSFP readout, occasional image artifacts including ghosting and banding were present, with one SASHA data set unanalyzable owing to artifacts. Banding artifacts are exacerbated in the presence of metallic implants or poor shimming and result in complex changes to signal intensities that may produce unreliable SASHA T_1 values. In the time-course data, the overall segment exclusion rate of 4% was comparable to 3% of exclusion rate reported for MOLLI (17), which is not surprising, given the similarity in single-shot bSSFP readouts used in both sequences.

T_1 Variability and Pulse Sequence Limitations

The normalized IQR (divided by median) is a metric of in vivo variability that includes the effects of SNR as well as other factors such as residual image misregistration from motion despite image registration and physiologic spatial variability in T_1, particularly in the patient population. At sufficiently high SNRs where the distribution of T_1 error is approximately normal, the CV is approximately equal to normalized IQR divided by 1.35. The average measured myocardial normalized IQR of 8.1% is thus approximately equivalent to a CV of 6.0%, comparable to the previously reported CVs of 6–8% for MOLLI in vivo (14,16).

In the worst case scenario where T_1 variability is owing entirely to noise alone, the Monte Carlo simulation results can be used to estimate lower bounds for SNR in the nonsaturated image using Figure 4. The average normalized IQR of 8.1 $\pm$ 3.0% in the myocardium and 6.0 $\pm$ 2.3% in the blood measured in vivo correspond to a minimum myocardial SNR of 49 and blood SNR of 74 at a heart rate of 60 bpm (marked data points, Fig. 4). A similar myocardial SNR value of 46 has been reported using a single-shot bSSFP readout (40). However, the use of smaller voxels and a T_2 preparation pulse in this referenced study suggests that higher SNR values are achievable.

At these estimated lower bounds of SNR for our study groups, Monte Carlo simulation results suggest that systematic overestimation of T_1 values is <0.5%, even at a heart rate of 100 bpm (Fig. 4). However, SNR may be diminished if flip angle is reduced owing to SAR limitations, if receiver coils are farther away from the myocardium in larger subjects, or other practical limitations in clinical settings. At low SNR values, SASHA T_1 values will be unreliable owing to systematic overestimation and increased variability as shown in Figure 4. Figure 4 can also be used to determine the minimum SNR required to attain a desired level of precision and accuracy in SASHA T_1 values. For example, if the normalized IQR is to be kept below 15% (equivalent to an 11% CV), with median error of <1% in the myocardium, a minimum SNR of 40 in the nonsaturated SASHA image must be attained.

Systematic overestimation at low SNR values is likely related to the Rician distribution, where the signal intensity in short TS time images is increased owing to the magnitude image reconstruction. It is possible that phase-sensitive reconstruction of SASHA images could therefore reduce systematic bias at low SNR values, as low signal intensities with noise would follow an unbiased Gaussian distribution instead.

Nonideal saturation pulse efficiency (η_{actual}) or incomplete spoiling may result in systematic errors in SASHA owing to the memory effect of incomplete saturation, and the SASHA sequence could also potentially be made more robust with the use of alternate saturation preparation pulses. However, nearly ideal saturation was measured in all phantoms, and a similarly robust in vivo saturation efficiency with a three-pulse composite saturation has been previously demonstrated at 3T (41). Therefore, the dependence on η_{actual} is not a practical limitation of the SASHA method.

As a bSSFP-based sequence, SASHA is sensitive to off-resonant frequency errors although simulations showed negligible best-fit T_1 errors for off-resonant frequencies from $\pm$96 Hz, which is 2.7 times the reported peak-to-peak variation of 70 Hz found across the myocardium at 1.5T (42). However, larger errors were found when off-resonance reached $\pm$0.36/TR ($\pm$137 Hz), which may be more likely at higher field strength as variations of up to 130 Hz have been reported at 3T (43). In these and other cases where off-resonance may be an issue, reducing the TR increases the range of absolute off-resonance frequencies where SASHA has minimal errors.

Study Limitations

Our study is limited by relatively small numbers of subjects imaged, particularly in the heart failure substudy. Although our results are consistent with the previous findings, further studies are needed to better characterize changes found in heart failure. Direct comparisons of SASHA to standard MOLLI sequences were not made in this study but are the subject of ongoing research.

As with the previous studies with in vivo calculations of the blood–tissue partition coefficient, this study makes several common assumptions about contrast agent kinetics. First, the contrast agent relaxivity is assumed not to differ between blood and tissue and thus cancels out in the calculation of λ although there is evidence to suggest that this may not hold true at higher field strengths (37). Second, it is assumed that contrast concentration between the blood and the tissue has reached equilibrium in all postcontrast measurements. Simulations have shown blood–tissue concentration equilibrium is reached 3 min after a contrast bolus for tissue blood flow above 0.5 mL·min^{-1}·g^{-1} (11), and a study comparing bolus contrast administration to a continuous infusion of contrast agent has shown similar λ values between them (5). However, it is possible that lower calculated λ values in this study for the time-course substudy before the 3-min mark are owing to nonequilibrium conditions. Finally, it is assumed that water exchange between tissue compartments is in the fast exchange regime (44).

In general, λ provides only a measure of extracellular volume fraction and not fibrosis itself. The extracellular volume fraction can be better estimated by correcting the partition coefficient for the blood hematocrit (7) although this was not available for subjects in this study. Although postcontrast myocardial T_1, λ, and extracellular volume fraction have been correlated with fibrosis in patients following heart transplantation (2) and with hypertrophic cardiomyopathy (3), other disease processes that increase extracellular volume would also present as reduced postcontrast myocardial T_1, increased λ, and increased extracellular volume fraction.

CONCLUSIONS

The proposed SASHA sequence allows for simple and fast in vivo measurements of myocardial and blood T_1 values. Numerical simulations suggest that the accuracy of measured T_1 values is independent of absolute T_1, T_2, heart rate, and flip angle, and spin echo experiments verified its accuracy in phantoms with physiologic T_1 and T_2 values. Potential sources of error include off-resonance, incomplete saturation preparation, and low SNR, which result in increasing variability and overestimation of T_1. SASHA is an excellent candidate for future T_1 mapping applications, but further studies and comparisons with existing T_1 mapping sequences need to establish their robustness in clinical patient populations.

APPENDIX

Origin of Apparent Changes in Saturation Efficiency in SASHA

The measured signal intensity in each saturation recovery single-shot acquisition (SASHA) image is determined

by a combination of saturation recovery preparation and the balanced steady-state free precession balanced steady-state free precession readout.

Saturation Recovery Preparation

The longitudinal magnetization for each SASHA image after saturation recovery preparation is characterized by a three-parameter exponential recovery curve:

$$M(0) = 1 - \eta_{\text{actual}} e^{-(TS-\Delta)/T_1} \qquad [A1]$$

where

η_{actual} is the saturation efficiency ($\eta_{\text{actual}} = 1$ for perfect saturation).

TS is the conventional definition of saturation recovery time, from the end of the saturation pulse to the center of k-space.

Δ is the time from the start of imaging to the center of k-space.

(TS-Δ) is the time from the end of the saturation pulse to the start of imaging.

For the nonsaturated image in SASHA, $M(0) = 1$.

Eq. A1 can be rewritten as:

$$M(0) = 1 - \eta_{\text{actual}} e^{-(TS-\Delta)/T_1}$$
$$M(0) = 1 - \eta_{\text{actual}} e^{\Delta/T_1 - TS/T_1}$$
$$M(0) = 1 - (e^{\Delta/T_1}) \eta_{\text{actual}} e^{-TS/T_1} \qquad [A2]$$

The offset factor Δ may also be expressed in terms of balanced steady-state free precession sequence parameters:

$$\Delta = (n-1)\text{TR} + \text{TE} \qquad [A3]$$

where

n is the number of RF pulses to the center of k-space.
TR is the repetition time.
TE is the echo time.

Effect of Balanced Steady-State Free Precession Readout

The signal intensity (magnitude of the transverse magnetization) of a spin-system after n RF pulses in a balanced steady-state free precession experiment may be approximated in the on-resonance case as (45):

$$S(n) = \left[\sin\left(\frac{\alpha}{2}\right)M(0) - M_{SS}\right]\lambda_1^n + M_{SS} \qquad [A4]$$

where

$$\lambda_1 = E_2 \sin^2\left(\frac{\alpha}{2}\right) + E_1 \cos^2\left(\frac{\alpha}{2}\right) \qquad [A5]$$

$$E_{1,2} = e^{-\text{TR}/T_{1,2}} \qquad [A6]$$

$$M_{SS} = \frac{\sqrt{E_2}(1 - E_1)\sin\alpha}{1 - (E_1 - E_2)\cos\alpha - E_1 E_2}, \qquad [A7]$$

M_{SS} is the steady state magnetization

$M(0)$ is the starting longitudinal magnetization after saturation recovery preparation.

TR is the repetition time.
α is the flip angle.

Eq. A4 can be rewritten in terms of the starting magnetization as:

$$S(n) = \left[\sin\left(\frac{\alpha}{2}\right)M(0) - M_{SS}\right]\lambda_1^n + M_{SS}$$

$$S(n) = \sin\left(\frac{\alpha}{2}\right)\lambda_1^n M(0) + [1 - \lambda_1^n]M_{SS}$$

$$S(n) = aM(0) + b \qquad [A8]$$

where

$$a = \sin\left(\frac{\alpha}{2}\right)\lambda_1^n \qquad [A9]$$

$$b = [1 - \lambda_1^n]M_{SS} \qquad [A10]$$

and a and b are constants determined by T_1, T_2, TR, flip angle, and n, the number of RF pulses to the center of k-space.

Equations A2 and A8 can be combined to yield the signal at the center of k-space, S, in terms of the three-parameter exponential recovery model:

$$S = aM(0) + b$$

$$S = a[1 - (e^{\Delta/T_1})\eta_{\text{actual}} e^{-TS/T_1}] + b$$

$$S = a + b - a(e^{\Delta/T_1})\eta_{\text{actual}} e^{-TS/T_1}$$

$$S = (a + b)\left[1 - \frac{a}{a+b}\left(e^{\Delta/T_1}\right)\eta_{\text{actual}} e^{-TS/T_1}\right]$$

$$S = A(1 - \eta_{\text{apparent}} e^{-TS/T_1}) \qquad [A11]$$

where

$$A = a + b \qquad [A12]$$

$$\eta_{\text{apparent}} = \left(\frac{a}{a+b} e^{\Delta/T_1}\right)\eta_{\text{actual}} \qquad [A13]$$

The apparent saturation efficiency (η_{apparent}) thus reflects not only the actual saturation efficiency (η_{actual}), but is also influenced by T_1, T_2, and pulse sequence parameters, as given by Eqs. A3, A5, A6, A7, A9, and A10.

Effect of a Flip Angle Distribution

A realistic slice excitation profile contains a distribution of flip angles and the total signal is a weighted sum of SASHA experiments performed with different flip angles. This can be represented as:

$$S' = \sum_{i=1}^{n} w_i S_i \qquad [A14]$$

where there are n experiments indexed by i, each with a different flip angle, and w_i are the weighting coefficients

that define the flip angle distribution. The signal intensity for each flip angle experiment is described by Eq. A11, where η_{apparent} is flip angle dependent, whereas the exponential term, $\exp(-TS/T_1)$, is not. Equation A14 can be rewritten as:

$$S' = \sum w_i[A_i(1 - \eta_{\text{apparent}_i}e^{-TS/T_1})]$$

$$S' = \sum w_iA_i - \left(\sum w_iA_i\eta_{\text{apparent}_i}\right)e^{-TS/T_1}$$

$$S' = \sum w_iA_i\left[1 - \left(\frac{\sum w_iA_i\eta_{\text{apparent}_i}}{\sum w_iA_i}\right)e^{-TS/T_1}\right]$$

$$S' = A'(1 - \eta'_{\text{apparent}}e^{-TS/T_1}) \qquad [\text{A15}]$$

where

$$A' = \sum w_iA_i \qquad [\text{A16}]$$

$$\eta'_{\text{apparent}} = \frac{\sum w_iA_i\eta_{\text{apparent}_i}}{\sum w_iA_i} \qquad [\text{A17}]$$

Therefore, the total signal intensity from a SASHA experiment with a flip angle distribution can still be represented by a three-parameter exponential recovery model.

ACKNOWLEDGMENTS

REFERENCES

1. Dall'armellina E, Piechnik SK, Ferreira VM, et al. Cardiovascular magnetic resonance by non contrast T1 mapping allows assessment of severity of injury in acute myocardial infarction. J Cardiovasc Magn Reson 2012;14:15.
2. Iles L, Pfluger H, Phrommintikul A, Cherayath J, Aksit P, Gupta SN, Kaye DM, Taylor AJ. Evaluation of diffuse myocardial fibrosis in heart failure with cardiac magnetic resonance contrast-enhanced T1 mapping. J Am Coll Cardiol 2008;52:1574–1580.
3. Flett AS, Hayward MP, Ashworth MT, Hansen MS, Taylor AM, Elliott PM, McGregor C, Moon JC. Equilibrium contrast cardiovascular magnetic resonance for the measurement of diffuse myocardial fibrosis: preliminary validation in humans. Circulation 2010;122:138–144.
4. Chow K, Flewitt JA, Green JD, Friedrich MG, Thompson RB. Characterization of Myocardial T1 and Partition Coefficient as a Function of Time after Gadolinium Delivery in Healthy Subjects. In Proceedings of the 19th Annual Meeting of ISMRM, Montreal, Canada, 2011. p. 1373.
5. Schelbert EB, Testa SM, Meier CG, et al. Myocardial extravascular extracellular volume fraction measurement by gadolinium cardiovascular magnetic resonance in humans: slow infusion versus bolus. J Cardiovasc Magn Reson 2011;13:16.
6. Messroghli DR, Plein S, Higgins DM, Walters K, Jones TR, Ridgway JP, Sivananthan MU. Human myocardium: single-breath-hold MR T1 mapping with high spatial resolution—reproducibility study. Radiology 2006;238:1004–1012.
7. Flacke SJ, Fischer SE, Lorenz CH. Measurement of the gadopentetate dimeglumine partition coefficient in human myocardium in vivo:

8. normal distribution and elevation in acute and chronic infarction. Radiology 2001;218:703–710.
8. Look D, Locker D. Time saving in measurement of NMR and EPR relaxation times. Rev Sci Instrum 1970;41:250–251.
9. Deichmann R, Haase A. Quantification of T1 values by SNAPSHOT-FLASH NMR imaging. J Magn Reson 1992;96:608–612.
10. Deichmann R, Hahn D, Haase A. Fast T1 mapping on a whole-body scanner. Magn Reson Med 1999;42:206–209.
11. Jerosch-Herold M, Sheridan DC, Kushner JD, Nauman D, Burgess D, Dutton D, Alharethi R, Li D, Hershberger RE. Cardiac magnetic resonance imaging of myocardial contrast uptake and blood flow in patients affected with idiopathic or familial dilated cardiomyopathy. Am J Physiol Heart Circ Physiol 2008;295:H1234–H1242.
12. Karlsson M, Nordell B. Analysis of the Look-Locker T(1) mapping sequence in dynamic contrast uptake studies: simulation and in vivo validation. Magn Reson Imaging 2000;18:947–954.
13. Gai N, Turkbey EB, Nazarian S, van der Geest RJ, Liu C-Y, Lima JAC, Bluemke DA. T1 mapping of the gadolinium-enhanced myocardium: adjustment for factors affecting interpatient comparison. Magn Reson Med 2011;65:1407–1415.
14. Messroghli DR, Radjenovic A, Kozerke S, Higgins DM, Sivananthan MU, Ridgway JP. Modified Look-Locker inversion recovery (MOLLI) for high-resolution T1 mapping of the heart. Magn Reson Med 2004; 52:141–146.
15. Messroghli DR, Greiser A, Fröhlich M, Dietz R, Schulz-Menger J. Optimization and validation of a fully-integrated pulse sequence for modified look-locker inversion-recovery (MOLLI) T1 mapping of the heart. J Magn Reson Imaging 2007;26:1081–1086.
16. Piechnik SK, Ferreira VM, Dall'Armellina E, Cochlin LE, Greiser A, Neubauer S, Robson MD. Shortened Modified Look-Locker Inversion recovery (ShMOLLI) for clinical myocardial T1-mapping at 1.5 and 3 T within a 9 heartbeat breathhold. J Cardiovasc Magn Reson 2010;12: 69.
17. Messroghli DR, Walters K, Plein S, Sparrow P, Friedrich MG, Ridgway JP, Sivananthan MU. Myocardial T1 mapping: application to patients with acute and chronic myocardial infarction. Magn Reson Med 2007;58:34–40.
18. Ugander M, Oki A, Hsu L-Y, Kellman P, Greiser A, Aletras A, Sibley C, Chen M, Bandettini W, Arai A. Extracellular volume imaging by magnetic resonance imaging provides insights into overt and subclinical myocardial pathology. Eur Heart J 2012;33:1268–1278.
19. Sparrow P, Messroghli DR, Reid S, Ridgway JP, Bainbridge G, Sivananthan MU. Myocardial T1 mapping for detection of left ventricular myocardial fibrosis in chronic aortic regurgitation: pilot study. AJR Am J Roentgenol 2006;187:W630–W635.
20. Chow K, Flewitt JA, Pagano JJ, Green JD, Friedrich MG, Thompson RB. MOLLI T1 Values Have Systematic T2 and Inversion Efficiency Dependent Errors. In Proceedings of the 20th Annual Meeting of ISMRM, Melbourne, Australia, 2012. p. 395.
21. Gai ND, Stehning C, Nacif M, Bluemke DA. Modified Look-Locker T1 evaluation using Bloch simulations: human and phantom validation. Magn Reson Med 2013;69:329–336.
22. Song T, Stainsby JA, Ho VB, Hood MN, Slavin GS. Flexible cardiac T(1) mapping using a modified look-locker acquisition with saturation recovery. Magn Reson Med 2012;67:622–627.
23. Wacker CM, Bock M, Hartlep AW, Beck G, van Kaick G, Ertl G, Bauer WR, Schad LR. Changes in myocardial oxygenation and perfusion under pharmacological stress with dipyridamole: assessment using T*2 and T1 measurements. Magn Reson Med 1999;41:686–695.
24. Higgins DM, Ridgway JP, Radjenovic A, Sivananthan UM, Smith MA. T1 measurement using a short acquisition period for quantitative cardiac applications. Med Phys 2005;32:1738–1746.
25. Jessup M, Brozena S. Heart failure. N Engl J Med 2003;348:2007–2018.
26. Mann DL. Mechanisms and models in heart failure: a combinatorial approach. Circulation 1999;100:999–1008.
27. Marquardt D. An algorithm for least-squares estimation of nonlinear parameters. J Soc Ind Appl Math 1963;11:431–441.
28. Foltz WD, Al-Kwifi O, Sussman MS, Stainsby JA, Wright GA. Optimized spiral imaging for measurement of myocardial T2 relaxation. Magn Reson Med 2003;49:1089–1097.
29. Kraft KA, Fatouros PP, Clarke GD, Kishore PR. An MRI phantom material for quantitative relaxometry. Magn Reson Med 1987;5:555–562.

30. Kellman P, Arai AE, McVeigh ER, Aletras AH. Phase-sensitive inversion recovery for detecting myocardial infarction using gadolinium-delayed hyperenhancement. Magn Reson Med 2002;47:372–383.

31. Klein S, Staring M, Murphy K, Viergever MA, Pluim JPW. elastix: a toolbox for intensity-based medical image registration. IEEE Trans Med Imaging 2010;29:196–205.

32. Cerqueira MD, Weissman NJ, Dilsizian V, Jacobs AK, Kaul S, Laskey WK, Pennell DJ, Rumberger JA, Ryan T, Verani MS, Imaging AHAWGoMSaRfC. Standardized myocardial segmentation and nomenclature for tomographic imaging of the heart: a statement for healthcare professionals from the Cardiac Imaging Committee of the Council on Clinical Cardiology of the American Heart Association. Circulation 2002;105:539–542.

33. Zur Y, Stokar S, Bendel P. An analysis of fast imaging sequences with steady-state transverse magnetization refocusing. Magn Reson Med 1988;6:175–193.

34. Janick PA, Hackney DB, Grossman RI, Asakura T. MR imaging of various oxidation states of intracellular and extracellular hemoglobin. AJNR Am J Neuroradiol 1991;12:891–897.

35. Lu H, Clingman C, Golay X, van Zijl PCM. Determining the longitudinal relaxation time (T1) of blood at 3.0 Tesla. Magn Reson Med 2004; 52:679–682.

36. Kawel N, Nacif M, Zavodni A, Jones J, Liu S, Sibley C, Bluemke D. T1 mapping of the myocardium: intra-individual assessment of post-contrast T1 time evolution and extracellular volume fraction at 3T for Gd-DTPA and Gd-BOPTA. J Cardiovasc Magn Reson 2012;14:26.

37. Sharma P, Socolow J, Patel S, Pettigrew RI, Oshinski JN. Effect of Gd-DTPA-BMA on blood and myocardial T1 at 1.5T and 3T in humans. J Magn Reson Imaging 2006;23:323–330.

38. Kawel N, Nacif M, Zavodni A, Jones J, Liu S, Sibley C, Bluemke D. T1 mapping of the myocardium: Intra-individual assessment of the effect of field strength, cardiac cycle and variation by myocardial region. J Cardiovasc Magn Reson 2012;14:27.

39. Kawel N, Nacif M, Santini F, Liu S, Bremerich J, Arai AE, Bluemke DA. Partition coefficients for gadolinium chelates in the normal myocardium: comparison of gadopentetate dimeglumine and gadobenate dimeglumine. J Magn Reson Imaging 2012;36:733–737.

40. Kellman P, Aletras AH, Mancini C, McVeigh ER, Arai AE. T2-prepared SSFP improves diagnostic confidence in edema imaging in acute myocardial infarction compared to turbo spin echo. Magn Reson Med 2007;57:891–897.

41. Kim D, Gonen O, Oesingmann N, Axel L. Comparison of the effectiveness of saturation pulses in the heart at 3T. Magn Reson Med 2008;59:209–215.

42. Reeder SB, Faranesh AZ, Boxerman JL, McVeigh ER. In vivo measurement of T*2 and field inhomogeneity maps in the human heart at 1.5 T. Magn Reson Med 1998;39:988–998.

43. Noeske R, Seifert F, Rhein KH, Rinneberg H. Human cardiac imaging at 3 T using phased array coils. Magn Reson Med 2000;44:978–982.

44. Donahue KM, Weisskoff RM, Burstein D. Water diffusion and exchange as they influence contrast enhancement. J Magn Reson Imaging 1997;7:102–110.

45. Scheffler K. On the transient phase of balanced SSFP sequences. Magn Reson Med 2003;49:781–783.